Small Structures

small structures

www.small-structures.com

RESEARCH ARTICLE OPEN ACCESS

Universal Fabrication of Graphene/Perovskite Oxide Hybrid Heterostructures

Yeongju Choi[1] | Seungjin Lee[2] | Dongwon Shin[1,3] | Sukhoon Sim[1] | Min-Hyoung Jung[2] | Dirk Wulferding[4] | Minjae Kim[1] | Jaesik Eom[1] | Myeesha Mostafa[3,5] | Wonhee Ko[3,5] | SeungNam Cha[1] | Jungseek Hwang[1] | Hu Young Jeong[6] | Ki Kang Kim[2] | Woo Seok Choi[1]

[1]Department of Physics, Sungkyunkwan University, Suwon, Republic of Korea | [2]Department of Energy Science, Sungkyunkwan University, Suwon, Republic of Korea | [3]Center for Advanced Materials and Manufacturing, The University of Tennessee, Knoxville, Tennessee, USA | [4]Department of Physics and Astronomy, Sejong University, Seoul, Republic of Korea | [5]Department of Physics and Astronomy, The University of Tennessee, Knoxville, Tennessee, USA | [6]Graduate School of Semiconductor Materials and Devices Engineering, Ulsan National Institute of Science and Technology, Ulsan, Republic of Korea

Correspondence: Ki Kang Kim (kikangkim@skku.edu) | Woo Seok Choi (choiws@skku.edu)

Received: 7 September 2025 | **Revised:** 26 November 2025 | **Accepted:** 28 November 2025

Keywords: chemical vapor deposition | graphene | hybrid heterostructures | perovskite oxides

ABSTRACT

Hybrid heterostructures composed of graphene and perovskite oxides provide a promising platform for exploiting synergetic interfacial functionalities. Conventional fabrication methods of the hybrid heterostructures rely on transferring graphene grown on metallic substrates—a process that is time-consuming, labor-intensive, and prone to introducing numerous defects. In this study, we present a universal, catalyst-free method for the direct growth of graphene on insulating substrates by using three different perovskite oxide substrates ($SrTiO_3$, $LaAlO_3$, and $(La_{0.18}Sr_{0.82})(Al_{0.59}Ta_{0.41})O_3$) using atmospheric chemical vapor deposition. Comprehensive characterization via Raman spectroscopy, X-ray spectroscopy, scanning probe microscopy, and electron microscopy confirmed the formation of a uniform, continuous monolayer graphene on all substrates. We identified that growth temperature critically governs graphene quality, as excessive active species may lead to secondary nucleation and the formation of multilayer graphene. Notably, all substrates shared the same optimal growth conditions. Low-temperature Raman spectroscopy and scanning tunneling microscopy of the graphene/$SrTiO_3$ hybrid heterostructure revealed cooperative phenomena, including substrate-induced lattice-phonon and electron–phonon coupling. Our work establishes a reproducible, transfer-free fabrication route for graphene/perovskite oxide hybrid heterostructures and provides empirical support for the universal growth of graphene on insulating substrates.

1 | Introduction

Hybrid heterostructures (HHs) composed of graphene and perovskite oxides serve as an emerging platform for exploiting interface-engineered cooperative functionalities [1, 2]. The platform hosts synergetic phenomena originating from the interaction between the two distinct materials, realizing properties that are not observable in conventional heterostructures [3–5]. A prominent example is the HH composed of the most well-studied 2D material, graphene, and the perovskite oxide $SrTiO_3$ (STO) which form one of the most celebrated hybrid heterointerfaces owing to its unique electronic interactions. Graphene (Gr)/STO HHs exhibit virtually noninteracting Dirac electrons [6], substantial voltage scaling of the quantum Hall effect, unexpected magnetoresistance, and a helical quantum Hall phase [7]. The graphene layer can also serve as a probe for investigating the light-modulated surface polarization and oxygen-vacancy-modulated dielectric responses of STO [8]. With the emergence of potential remote epitaxy, Gr/STO HHs have also been utilized to fabricate free-standing perovskite

oxide membranes [9–12]. However, with few exceptions, most studies have relied on graphene transfer to fabricate the HHs. This is because graphene typically grows preferentially on metallic substrates such as Cu or Ni, where catalytic activity facilitates chemical vapor deposition (CVD), unless exfoliated [13–16]. Although growth on metallic substrates generally yields high-quality graphene, the subsequent transfer process often introduces unintended defects and results in low yield. Moreover, the process is time-consuming, involves complex manual handling, and is limited in the achievable lateral size.

To overcome these challenges, the direct growth of graphene on perovskite oxide substrates can be envisaged. Conventionally, direct graphene growth has been demonstrated on catalytically active metal substrates. However, achieving direct growth of 2D layers including graphene on insulating substrates remains challenging [17]. On metals, catalytic activity facilitates the decomposition of carbon precursors, which promotes graphene formation [13–16, 18]. In contrast, insulating substrates lack such activity, resulting in different growth mechanisms [19]. Consequently, graphene growth on these substrates tends to have a narrow growth window and a low growth rate [20–26]. In the absence of catalysis, thermal decomposition is expected to dominate, suggesting that graphene growth may be relatively insensitive to specific insulating substrate used. Therefore, assuming the substrates remain stable under growth conditions, establishing universal growth conditions for HH fabrication may be possible.

Given that graphene growth on insulating substrates might be relatively independent of substrate choice, we herein demonstrate the universal fabrication of graphene/perovskite oxide HHs using a simple atmospheric pressure chemical vapor deposition (APCVD) process. We used (001)-oriented STO, $LaAlO_3$ (LAO), and $(La_{0.18}Sr_{0.82})(Al_{0.59}Ta_{0.41})O_3$ (LSAT) perovskite oxide substrates, as they are widely used and thermally stable up to at least 1100°C. Ar, H_2, and CH_4 gases were used as precursors in the APCVD process, which was conducted at relatively high temperatures (>1050°C) to enable thermal decomposition. Upon identifying a narrow but optimal growth window, we achieved uniform graphene growth across the entire $5 \times 5\ mm^2$ substrate area. The key factors for the high-quality graphene growth were precise control of temperature and precursor flow rate. Most importantly, we identified a set of growth conditions that were universally applicable to STO, LAO, and LSAT, thereby potentially eliminating the need for transfer process in HH fabrications.

2 | Results and Discussion

2.1 | HH Fabrication

We identified an optimal growth condition applicable to Gr/STO [9, 23], Gr/LAO, and Gr/LSAT HHs. We controlled temperature, precursor flow rate, and growth time, in the APCVD process. The optimal conditions were found to be a temperature of 1070°C, a mixed gas of Ar, H_2, and CH_4 with a flow rate ratio of 250 : 10 : 8 sccm, and a growth time of 1–3 h (see Methods section). In this study, CH_4 was selected as the carbon source to ensure consistency with established precedents for catalyst-free graphene growth on insulating substrates [9, 20–25]. While C_2H_6 (ethane) is a possible alternative, its higher reactivity is anticipated to promote unintended carbon aggregation or graphene adlayers [27]. The overall quality of the HHs was evaluated by assessing the physical characteristics of graphene, including uniformity, and cleanliness of the surfaces and interfaces.

2.2 | Raman and X-ray Spectroscopies

Under optimal growth conditions, the HHs exhibit uniform graphene quality. The Raman spectra in Figure 1 demonstrate the uniformity of the Gr/STO and Gr/LAO HHs [28]. We subtracted

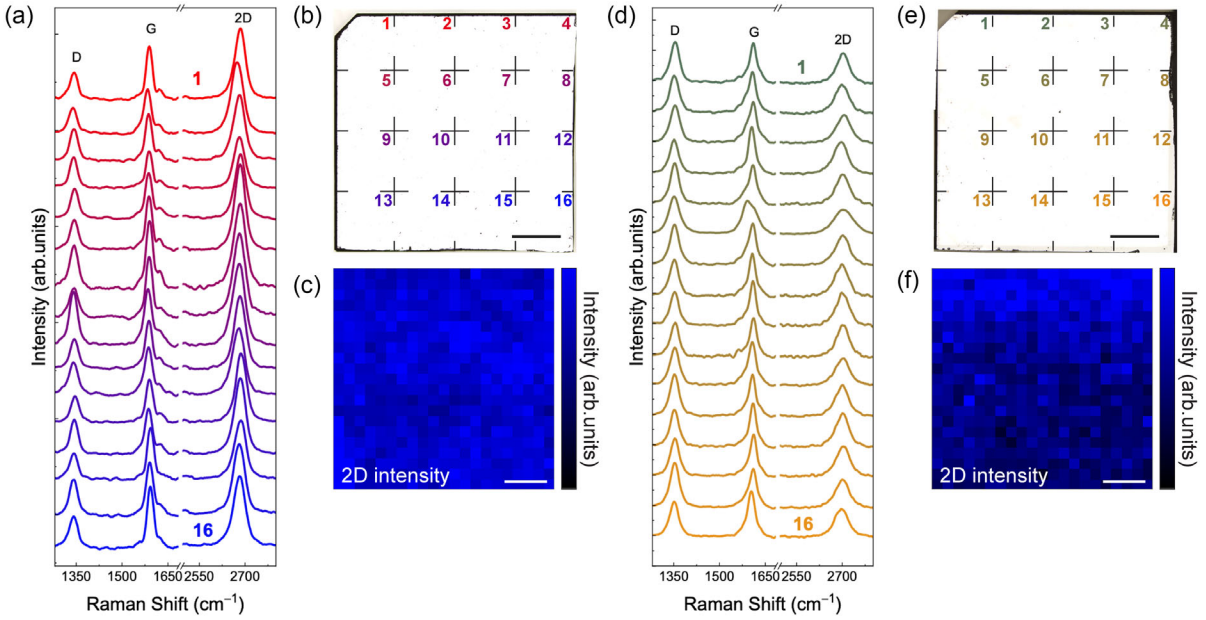

FIGURE 1 | Uniform graphene growth on (a–c) STO and (d–f) LAO substrates. (a,d) Representative Raman spectra from 16 evenly spaced points on the HH surfaces, demonstrating graphene uniformity. The positions of the measured points are marked as different colors and numbers on the optical microscopy images in (b,e) (scale bar: 1 mm). (c,f) 2D intensity mappings of Raman spectra from the HHs taken at random positions (scale bar: 4 μm).

the substrate spectra from the HH spectra to eliminate the substrate contributions, using confocal Raman spectroscopy (Figure S1, Supporting Information) [29]. Figure 1a,1d show the Raman spectra measured at equal lateral intervals (as indicated in Figure 1b,e), across the $5 \times 5\ mm^2$ Gr/STO and Gr/LAO HHs, respectively. Figure 1b,e are the optical microscope images of the grown graphene samples; the corresponding images without numbers or boundary lines for better visualizations are shown in Figure S2. We also analyzed the Raman spectra statistically, as shown in Figure S3, manifesting small deviation between the spectra. Raman spectroscopy for the Gr/LSAT HH is shown in Figure S4a. Although a strong fluorescence feature at high energy from the LSAT substrate (Figure S1c, Supporting Information) obscured part of the analysis, similar uniformity was confirmed (Figure S4a, Supporting Information). All Raman spectra across the substrates exhibited the characteristic D, G, and 2D peaks of graphene. In Figure 1c,f, we mapped the 2D peak intensity to visualize the spatial uniformity of the Gr/STO and Gr/LAO HHs. The 2D peak intensity was nearly uniform across the HHs, with the spatial resolution limited by the laser spot size (~600 nm). The G peak intensity maps also indicated uniformity across the samples (Figure S5, Supporting Information). We note that Raman spectra of graphene may vary across different substrates, possibly due to dielectric screening and strain effects originating from differences in thermal expansion coefficients (TECs) [30–32]. Therefore, although a 2D/G intensity ratio below two is typically taken to indicate polycrystalline nature or lower graphene quality on conventional SiO_2/Si substrates, this criterion may not apply directly to Gr/perovskite oxide HHs [23]. Nevertheless, our Raman spectroscopy results clearly demonstrate that the graphene was uniformly grown across all perovskite substrates used.

Similarly, near-edge X-ray absorption fine structure (NEXAFS) spectra of the HHs confirmed the quality of the graphene layer [33, 34]. C *K*-edge NEXAFS spectra reveal clear features of σ^* C═C bonding at 292 eV and π^* C─C bonding at 286 eV, as shown in Figure S6. Considering that the measurement was performed vertically, the relatively sharp feature and higher intensity of σ^* peak compared to those of π^* peak indicate the growth of graphene, rather than other phases, such as graphene oxide. The peak features originating from graphene were nearly identical regardless of the substrate used, indicating a similar quality of graphene.

2.3 | Scanning and Electron Microscopies

Micrometer- and atomic-scale microscopy confirm the high structural quality of the HH surfaces and interfaces. Scanning electron microscopy (SEM) revealed clean surfaces at the micrometer scale under optimal growth conditions (Figure 2a,b,d). When the growth conditions deviated from the optimum, defects, residues, or overgrowth readily appeared on the surface (Figure S7, Supporting Information). For the Gr/STO HH, high-magnification SEM imaging (Figure 2b) was possible because the STO substrate became metallic with the introduction of oxygen vacancies under the reducing, high-temperature conditions of APCVD [35]. At higher magnification, we observed several lines on the surface, previously interpreted in the literature as graphene wrinkles or grain boundaries [36–39]. Atomic force microscopy (AFM) images revealed similar line structures atop the step-and-terrace structures of the substrates, as shown in Figure 2c,e, for Gr/STO and Gr/LAO HHs, respectively. The surfaces of Gr/STO and Gr/LAO HHs were atomically flat, with RMS roughness values of 0.319 and 0.274 nm, respectively (Figure S8, Supporting Information), aside from the inherent step-and-terrace structures (~0.4 nm) of the substrates (Figure S9, Supporting Information). The characteristic lines exhibited heights of ~1.2 and ~0.6 nm for the Gr/STO and Gr/LAO HHs, respectively. The Gr/LSAT HH also exhibited similar surface quality and the line features in AFM (Figure S8c, d,g,j, Supporting Information), although an extensive number of particulates originating from the annealed substrate were observed (Figure S9c, Supporting Information) [40].

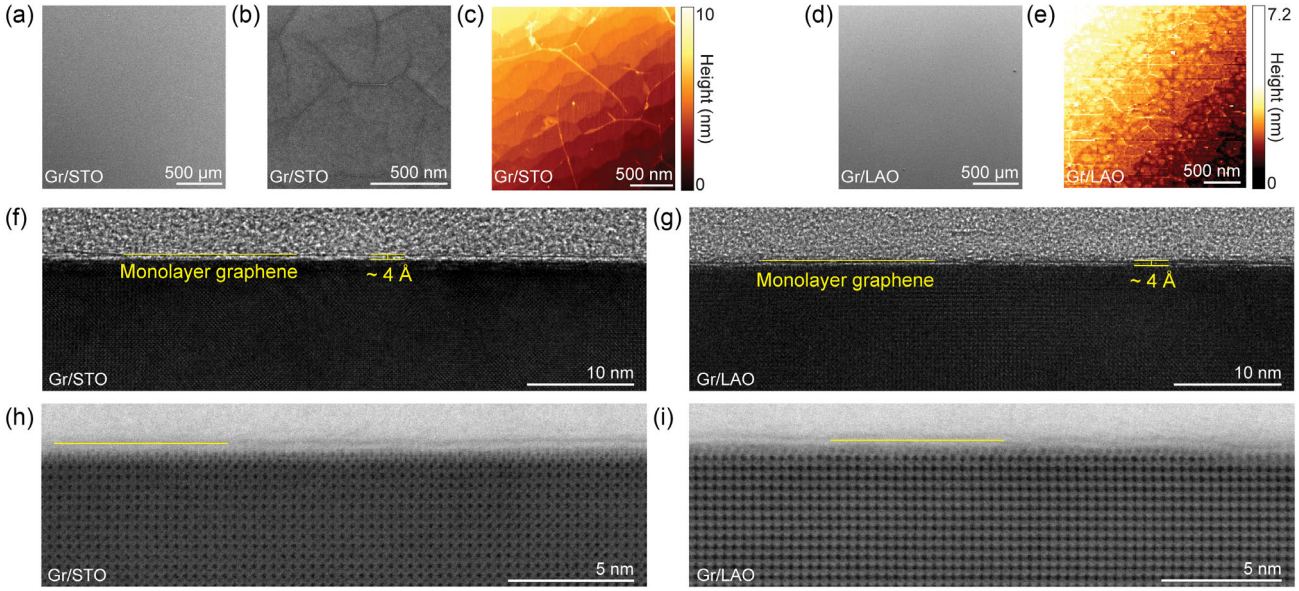

FIGURE 2 | Micrometer- and atomic-scale microscopy images of HHs with (a–c,f,h) STO and (d,e,g,i) LAO substrates. (a,b,d) SEM and (c,e) AFM topography images of HH surfaces. The dark lines in the SEM image (b) and the bright lines in the AFM images (c,e) represent graphene wrinkles. Cross-sectional (f,g) TEM and (h,i) STEM images of Gr/STO and Gr/LAO HHs, respectively. Dark lines on the crystal structures indicate monolayer graphene (highlighted with yellow horizontal lines).

Additionally, lateral force microscopy (LFM) (Figure S10, Supporting Information) revealed similar frictional distributions, and conductive AFM (C-AFM) (Figure S11, Supporting Information) demonstrated uniform conductivity across the HHs, both supporting the high surface quality of the graphene.

Cross-sectional transmission electron microscopy (TEM) and scanning TEM (STEM) confirmed predominant monolayer graphene growth in the HHs. The dark horizontal lines observed atop the perovskite oxide surface in all TEM (Figures 2f,g and S4b, Supporting Information) and STEM images (Figures 2h,i and S4c, Supporting Information) indicate successful formation of monolayer graphene on STO, LAO, and LSAT substrates [27, 41]. The distance between graphene and the top perovskite oxide surface was approximately 4 Å with small variation, consistent with previous reports on graphene grown on SiO_2 and Cu substrates [42, 43]. Multilayer graphene was rarely observed only in regions containing extended surface defects (Figure S12, Supporting Information), suggesting that a self-limiting mechanism governs graphene formation on clean perovskite oxide surfaces.

We further identified graphene wrinkles, which appeared as characteristic line structures in the SEM and AFM images (Figure 2b,c,e). Cross-sectional TEM and STEM of the Gr/STO HH showed that the wrinkles had a height of ~1.4 nm (Figure S13, Supporting Information), consistent with the AFM observations (Figure S8e, Supporting Information). The images indicate that the monolayer graphene remains continuous even in the presence of wrinkles, with no evident cracks or disruptions. We speculate that these wrinkles result from the TEC mismatch between graphene and the substrates [44–46]. During the post-growth cooling process, graphene expands while the perovskite oxide substrate contracts, leading to natural wrinkle formation. While such feature may raise concerns about the quality of the graphene surface, the TEC-induced wrinkle is a common phenomenon, even observed in high-quality, uniform graphene grown on Cu foils [47]. Overall, microscopic observations, including SEM, AFM, LFM, C-AFM, TEM, and STEM, confirm the successful growth of high-quality monolayer graphene on perovskite oxide substrates under optimized conditions.

2.4 | Temperature-Dependent Growth

In optimizing the growth conditions for HHs, temperature was found to be one of the most critical parameters, and the observed trends were consistent across all the substrates used in this study. We first noted that graphene began to grow above 1060°C. As shown in Figure 3a, no uniform graphene features were observed at 1060°C. At 1070°C, graphene grew uniformly across the substrate, with visible wrinkles (Figure 3b). At temperatures above 1070°C, adlayers (relatively bright regions) began forming atop the graphene surface (Figure 3c–e). This secondary nucleation is typically associated with inferior graphene quality when grown on dielectric substrates [9, 24, 27, 48, 49]. A similar trend was experimentally observed for graphene grown on LAO substrates, as shown in Figure 3f–j. Raman spectra of HHs fabricated at various temperatures corroborated the AFM results, with optimal spectra corresponding to samples grown at 1070 and 1080°C (Figure S14, Supporting Information). We also observed that above 1070°C, defect density and size increased with growth time (Figure S15, Supporting Information). However, at the optimal temperature of 1070°C, a self-limiting mechanism seemed to suppress defect formation above the monolayer graphene, even with prolonged growth durations (Figure S16, Supporting Information). Other factors, such as hydrogen flow rate and substrate surface roughness, also influenced the growth process (Supplementary Note 1; Figure S12 and S17, Supporting Information). Similar to temperature dependence, suboptimal values for these parameters promoted secondary nucleation, which hindered the formation of uniform, defect-free HHs. Therefore, suppressing secondary nucleation is key to achieving high-quality HH growth.

Secondary nucleation can result from oversupply of active species or surface reactions that promote overgrowth. The APCVD growth of graphene on insulating perovskite oxide surfaces can be described by a two-step mechanism: generation of active carbon precursors, followed by graphene formation from these precursors [19, 50, 51]. While purely thermal decomposition of CH_4 is unlikely at our growth temperature (1070°C) on an insulating substrate [50–52], the decomposition maybe driven by a gas–phase reaction. Consistent with a recent computational study [19], this mechanism considers hydrogen radicals (H·), abundantly supplied in our APCVD environment, collide with CH_4 molecules to facilitate the generation of CH_3· radicals ($H\cdot + CH_4 \rightarrow CH_3\cdot + H_2$). This reaction has a sufficiently low activation energy (45–60 kJ/mol) to be readily activated at our experimental temperature [19]. The first step is thus a gas-phase reaction dependent on the gas temperature, whereas the second step is a surface reaction primarily governed by the substrate temperature.

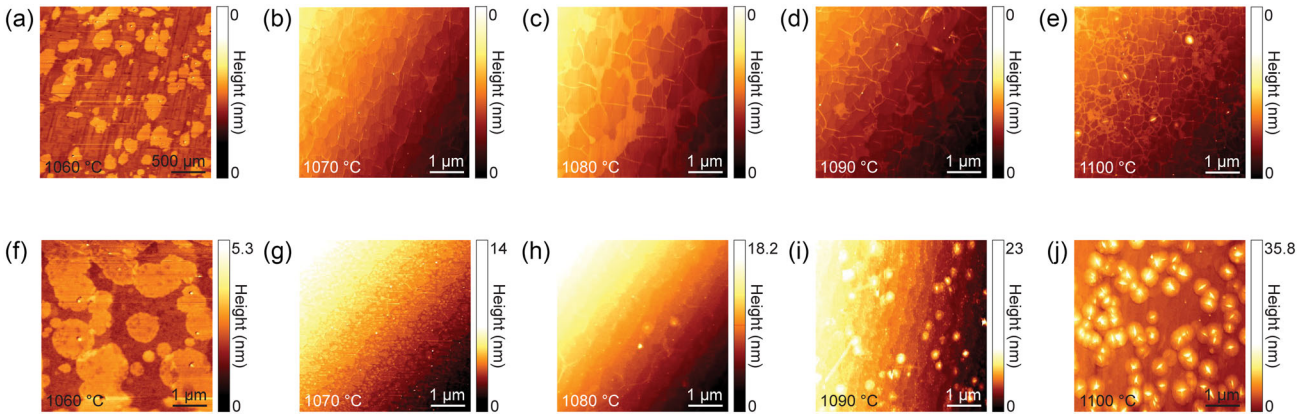

FIGURE 3 | Temperature-dependent growth behavior of the HHs. AFM topography images of (a–e) Gr/STO and (f–j) Gr/LAO HHs. As the growth temperature increases, adlayer or secondary nucleation becomes more prominent.

To elucidate this mechanism, we positioned substrates at various locations within the APCVD quartz tube at 1100°C, as shown in Figure 4a. As the substrate is positioned near the inlet (Position 1), growth does not initiate, because the temperature is not sufficiently high. As the substrate is positioned toward the center of the tube (position 2), an ideal growth condition is achieved. The center of the tube apparently experiences the highest temperature, which enhances both the CH_3· generation and the surface reaction rate. Hence, as the substrate is positioned beyond the center of the tube (position 3), overgrowth of graphene takes place. Although CH_3· radical generation is most active near the center, the flow direction causes CH_3· radicals to accumulate toward the outlet. SEM images showed that the sample placed closest to the outlet (Position 4) exhibited the most severe secondary nucleation, indicating that excessive CH_3· radicals promote overgrowth. To confirm the effect of radical oversupply, we increased the CH_4 precursor flow rate from the optimal 8–16 sccm. This adjustment led to the formation of graphene adlayers, as seen in SEM and AFM images (Figure S18, Supporting Information). Hence, the relatively low, optimal 8 sccm of CH_4 flow rate is a necessary condition. Based on previous studies [9, 19, 24, 27, 48, 49] and our own experimental results, graphene growth on an insulating substrate has a relatively slow growth rate compared to that on a metallic substrate. Therefore, if the CH_3· radical supply is too high, it would overwhelm the slow surface kinetics, causing secondary nucleation and adlayer formation as demonstrated in Figures 4e and S18. Consequently, a relatively low CH_4 partial pressure is required to balance the gas-phase precursor supply with the slow surface kinetics, enabling self-limiting process of monolayer graphene growth for the HH.

Finally, the temperature dependence of graphene growth was consistent across STO, LAO, and LSAT substrates, with no major differences observed among these insulating substrates [20, 21, 25, 27]. The observation that STO shares identical growth temperature windows and defect trends with LAO despite the presence of oxygen vacancies (Figure 3) indicates that these vacancies exert negligible influence on the growth mechanism (Supplementary Note2). This consistency provides strong experimental validation for our proposed gas-phase mechanism. Being independent of the specific oxide substrate chemistry, this observation explains the similar growth behaviors. These findings further highlight the universal applicability of APCVD for fabricating HHs and underscore the importance of controlling CH_3· radical concentration.

2.5 | Low-Temperature Raman Spectroscopy and Scanning Tunneling Microscopy

A structural phase transition in STO at low temperature is reflected in the phonon spectra of graphene, providing an example of the synergetic behavior. To probe the cooperative interfacial interactions, we measured low-temperature Raman spectra of the HH. The antiferrodistortive (AFD) transition of STO, which occurs at ~100 K depending on the oxygen stoichiometry of STO, results in a change in its TEC [53–55]. As a consequence, the strain exerted onto graphene is expected to vary. Figure 5 shows the temperature-dependent positions of the G and 2D peaks of the Gr/STO HH. Both peaks shift to higher frequencies as the temperature decreases. Notably, the slope of the G peak shift changes sign at ~100 K. The 2D peak also exhibits an anomaly near that temperature, although less pronounced. Below the AFD transition, the TEC of STO exhibits minimal temperature dependence, which is also reflected in the Raman spectra of graphene. In contrast, Gr/LAO HH does not show any significant temperature-dependent behavior (Figure S19, Supporting Information), supporting that the observed Raman peak shifts in Gr/STO HH primarily arise from substrate-induced thermo-mechanical interactions in the HHs.

To visualize the atomic lattice and investigate the electronic structure of the Gr/STO HH, we performed scanning tunneling microscopy/spectroscopy (STM/S) study at 4.2 K. Figure 5e presents a $5 \times 5\,nm^2$ topographic image with atomic resolution, clearly resolving the honeycomb lattice of graphene. Figure 5f displays the characteristic differential conductance (dI/dV) spectrum of the surface. The spectrum shows strong asymmetry, with significantly reduced dI/dV on the negative bias side compared to the positive side, indicating that the Dirac point of graphene lies

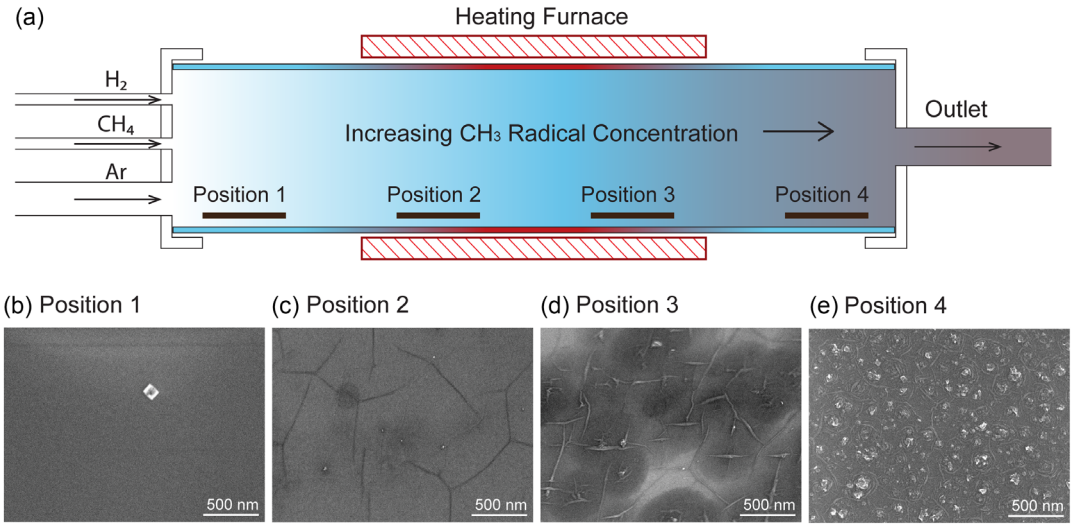

FIGURE 4 | Position dependent growth behavior of Gr/STO HHs in APCVD at 1100°C. (a) Schematic representation of different growth positions within the APCVD quartz tube. The temperature peaks at the center of the tube, whereas CH_3· radical concentration is highest near the outlet (position (e)). (b–e) SEM images of HH surfaces corresponding to the positions 1–4 in (a).

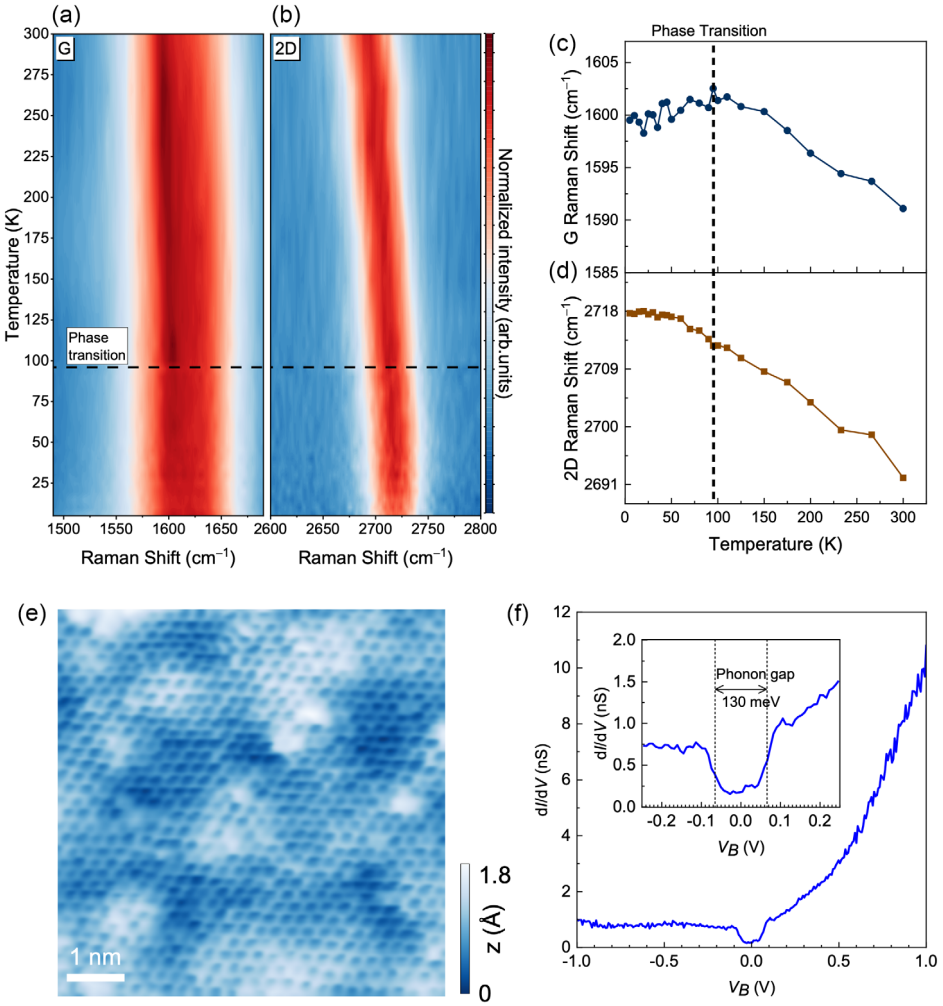

FIGURE 5 | Low temperature Raman and STM/S Analyses of Gr/STO HH. (a,b) Color contour plots of the temperature-dependent Raman spectra around the (a) G and (b) 2D peaks. AFD phase transition of STO occurs at approximately 100 K. (c,d) Peak positions of the G and 2D peaks as a function of temperature. (e) Topographic image of Gr/STO HH with atomic resolution ($V_B = 100$ mV, $I_t = 1$ nA) obtained by STM. (f) dI/dV spectrum of Gr/STO HH obtained by STS. The inset shows the same spectra enlarged around the Fermi level.

below the Fermi energy owing to substantial electron doping induced by HH formation. Additionally, a gap-like feature appears at the Fermi level. The width of the gap is approximately 130 mV, consistent with the phonon-induced inelastic electron tunneling spectra [56–58]. This observation suggests that the local phononic structure of graphene is discernible by STS, providing another example of the synergetic behavior in the Gr/STO HH. While the measurement temperature of 4.2 K may be too high to resolve strain-induced shifts in phonon energy, future studies at lower temperatures would make such features observable.

3 | Conclusion

In summary, we have demonstrated a universal, catalyst-free fabrication method for Gr/perovskite oxide (STO, LAO, and LSAT) HHs using an optimized APCVD process. Spectroscopic and microscopic characterization confirmed that all the HHs possessed uniform and continuous monolayer graphene. A systematic parameter scan revealed a narrow, yet robust growth window that governs the universal formation of optimal HHs. This further suggests that the same optimal conditions may be applicable to other insulating, high-temperature-stable substrates. In addition, our study goes beyond simple fabrication of the HHs. Low-temperature spectroscopy revealed thermo-mechanical and electron–phonon interactions between graphene and the STO substrate, proving multiple evidence of the synergetic behavior in the HH. Our work establishes a transfer-free method for HH fabrication and offers empirical evidence for universal graphene growth principles on insulating substrates.

4 | Experimental Section/Methods

4.1 | Pretreatment of Perovskite Oxide Substrates

(001)-oriented STO, LAO, and LSAT substrates (Shinkosha, Japan) were selected as growth substrates. To obtain step-terrace structures on the surface, the substrates were annealed under AP conditions at temperatures ranging from 950 to 1250°C, depending on the substrate type [40, 59]. Prior to annealing, STO and LAO substrates were chemically etched using a buffered oxide etchant for 15 s to selectively remove surface contamination and the native amorphous oxide layer, thereby promoting the formation of atomically smooth surface and well-defined step edges during subsequent annealing.

4.2 | Growth of Graphene on Perovskite Oxides

The pretreated substrates were loaded into an APCVD chamber, which was purged for 20 min using high-purity argon (Ar, >99.9999%) and hydrogen (H_2, >99.999%) gases at flow rates of 250 and 10 sccm, respectively, to eliminate residual air and prevent unwanted reactions. Then, the temperature was rapidly ramped up to 1070°C within 10 min. The specified temperature refers to the furnace setpoint at the center of the chamber measured by an external thermocouple. The substrates were annealed at this temperature for 15 min to remove native oxides and carbonaceous impurities from their surfaces. After annealing, methane gas (CH_4, >99.999%) was introduced at a flow rate of 8 sccm for 1–3 h to facilitate graphene growth. After the growth, the system was naturally cooled down to room temperature.

4.3 | Spectroscopy Measurements

The graphene film was analyzed using confocal Raman spectroscopy (532 nm; XperRAM 200, NanoBase, Korea). As the Raman signals from the substrate overlapped with those from graphene, the substrate spectrum was subtracted from the total spectrum at each corresponding position [29]. To account for intensity differences, both spectra were normalized by their respective standard deviations. Low-temperature Raman spectra were obtained using a custom-built Raman system with a 532 nm continuous-wave laser. Near-edge X-ray absorption fine structure (NEXAFS) measurements were conducted at the C *K*-edge (0° incidence, 300 K) to probe graphene-specific features, performed at the 6A beamline of the Pohang Accelerator Laboratory (PAL), Korea.

4.4 | Microscopy Measurements

The HH samples were characterized using AFM (XE7, Park Systems, Korea) to assess topography and lateral force for investigating graphene and substrate morphology. Current mapping was performed to evaluate local conductance. Surface morphology and structural characteristics of the as-grown graphene films were evaluated by field-emission scanning electron microscopy (FE-SEM; JSM-7600F, JEOL, Japan), where defects, adlayers, or graphene wrinkles produced variations in secondary electron emission. An optical microscope was used to identify measurement areas and to verify the uniformity of the Raman spectra across the HHs. Cross-sectional specimens were prepared using a dual-beam focused ion beam (FIB) system (FEI Helios NanoLab 450). The FIB sampling process was conducted at 30 kV (90 pA) and refined at 5 kV (56 pA) to minimize the formation of amorphous layers caused by beam damage. TEM and STEM were performed using a JEM-ARM200CF equipped with a double Cs corrector, operating at an accelerating voltage of 200 kV and under ultrahigh vacuum conditions.

4.5 | Scanning Tunneling Microscopy/Spectroscopy

STM/STS measurements were performed using a Unisoku USM-1300 STM operated at ultrahigh vacuum ($<5\times10^{-10}$ Torr) and 4.2 K. To clean the surface, the sample was annealed at 400°C for 1 h inside the STM chamber prior to measurement. Mechanically ground PtIr wires were used as STM tips, which were further prepared on a Au(111) crystal by performing field emission, followed by gentle poking and pulsing on a clean surface. To acquire dI/dV spectra, we used a conventional lock-in technique with a modulation amplitude of 1 mV and modulation frequency of 873 Hz.

Author Contributions

Yeongju Choi: data curation (lead), formal analysis (lead), investigation (lead), validation (equal), visualization (lead), writing – original draft (lead), writing – review and editing (lead). **Seungjin Lee**: data curation (lead), formal analysis (lead), investigation (lead), validation (equal), writing – review and editing (equal). **Dongwon Shin**: data curation (lead), formal analysis (lead), investigation (lead), validation (equal), visualization (equal), writing – review and editing (equal). **Sukhoon Sim**: investigation (supporting), writing – original draft (supporting), writing – review and editing (supporting). **Min-Hyoung Jung**: data curation (lead), investigation (lead), validation (equal), visualization (lead), writing – review and editing (supporting). **Dirk Wulferding**: data curation (lead), formal analysis (lead), methodology (equal), validation (supporting), visualization (supporting), writing – original draft (equal), writing – review and editing (supporting). **Minjae Kim**: data curation (supporting), investigation (supporting), writing – review and editing (supporting). **Jaesik Eom**: data curation (supporting), formal analysis (supporting), methodology (supporting), visualization (supporting), writing – review and editing (supporting). **Myeesha Mostafa**: data curation (supporting), investigation (supporting), writing – review and editing (supporting). **Wonhee Ko**: data curation (equal), funding acquisition (equal), methodology (equal), supervision (equal), validation (equal), visualization (supporting), writing – original draft (supporting), writing – review and editing (supporting). **SeungNam Cha**: funding acquisition (equal), methodology (supporting), supervision (supporting), writing – review and editing (supporting). **Jungseek Hwang**: supervision (supporting), validation (equal), writing – review and editing (equal). **Hu Young Jeong**: investigation (equal), methodology (lead), supervision (lead), validation (equal), visualization (lead), writing – review and editing (supporting). **Ki Kang Kim**: conceptualization (lead), funding acquisition (lead), methodology (lead), project administration (lead), supervision (lead), validation (lead), writing – original draft (equal), writing – review and editing (equal). **Woo Seok Choi**: conceptualization (lead), funding acquisition (lead), project administration (lead), supervision (lead), validation (lead), visualization (equal), writing – original draft (lead), writing – review and editing (lead).

Acknowledgments

We appreciate W.-s. Noh for his assistance at PAL (beamline 6A) and H. S. Kum for insightful discussion.

Funding

This study was supported by the National Research Foundation of Korea (Grant 2021R1A2C2011340, RS-2023-00220471, RS-2023-00281671, RS-2022-R1A2C2011109, RS-2022-NR068223, 2022R1A2C2091475, and RS-2024-00439520), the National Science Foundation Materials Research Science and Engineering Center program (Grant DMR-2309083), the Institute of Applied Physics of Seoul National University, and Sejong University.

Conflicts of Interest

The authors declare no conflicts of interest.

Data Availability Statement

The data that support the findings of this study are available from the corresponding author upon reasonable request.

References

1. D. Shin, H. Kim, S. J. Hong, et al., "Electrically Tunable Spin Exchange Splitting in Graphene Hybrid Heterostructure," *Advanced Functional Materials* 34, no. 11 (2024): 2311287, https://doi.org/10.1002/adfm.202311287.

2. K. T. Kang, J. Park, D. Suh, and W. S. Choi, "Synergetic Behavior in 2D Layered Material/Complex Oxide Heterostructures," *Advanced Materials* 31, no. 34 (2019): 1803732, https://doi.org/10.1002/adma.201803732.

3. J.-F. Ge, Z.-L. Liu, C. Liu, et al., "Superconductivity above 100 K in Single-Layer FeSe Films on Doped $SrTiO_3$," *Nature Materials* 14, no. 3 (2015): 285, https://doi.org/10.1038/nmat4153.

4. M. Hammad, S. Angel, A. K. Al-Kamal, et al., "Synthesis of Novel $LaCoO_3$/Graphene Catalysts as Highly Efficient Peroxymonosulfate Activator for the Degradation of Organic Pollutants," *Chemical Engineering Journal* 454 (2023): 139900, https://doi.org/10.1016/j.cej.2022.139900.

5. C. Xie, Y. Wang, Z.-X. Zhang, D. Wang, and L.-B. Luo, "Graphene/Semiconductor Hybrid Heterostructures for Optoelectronic Device Applications," *Nano Today* 19 (2018): 41, https://doi.org/10.1016/j.nantod.2018.02.009.

6. N. J. G. Couto, B. Sacépé, and A. F. Morpurgo, "Transport through Graphene on $SrTiO_3$," *Physical Review Letters* 107, no. 22 (2011): 225501, https://doi.org/10.1103/PhysRevLett.107.225501.

7. L. Veyrat, C. Déprez, A. Coissard, et al., "Helical Quantum Hall Phase in Graphene on $SrTiO_3$," *Science* 367, no. 6479 (2020): 781, https://doi.org/10.1126/science.aax8201.

8. K. T. Kang, H. Kang, J. Park, D. Suh, and W. S. Choi, "Quantum Conductance Probing of Oxygen Vacancies in $SrTiO_3$ Epitaxial Thin Film Using Graphene," *Advanced Materials* 29, no. 18 (2017): 1700071, https://doi.org/10.1002/adma.201700071.

9. K. S. Kim, J. E. Kang, P. Chen, et al., "Atomic Layer-by-Layer Etching of Graphene Directly Grown on $SrTiO_3$ Substrates for High-Yield Remote Epitaxy and Lift-Off," *APL Materials* 10, no. 4 (2022): 041105, https://doi.org/10.1063/5.0087890.

10. C. S. Chang, K. S. Kim, B.-I. Park, et al., "Remote Epitaxial Interaction through Graphene," *Science Advances* 9, no. 42 (2023): eadj5379, https://doi.org/10.1126/sciadv.adj5379.

11. S. A. Lee, J.-Y. Hwang, E. S. Kim, S. W. Kim, and W. S. Choi, "Highly Oriented $SrTiO_3$ Thin Film on Graphene Substrate," *ACS Applied Materials & Interfaces* 9, no. 4 (2017): 3246, https://doi.org/10.1021/acsami.6b12258.

12. H. Yoon, T. K. Truttmann, F. Liu, et al., "Freestanding Epitaxial SrTiO3 Nanomembranes via Remote Epitaxy Using Hybrid Molecular Beam Epitaxy," *Science Advances* 8, no. 51 (2022): eadd5328, https://doi.org/10.1126/sciadv.add5328.

13. S. Xu, L. Zhang, B. Wang, and R. S. Ruoff, "Chemical Vapor Deposition of Graphene on Thin-Metal Films," *Cell Reports Physical Science* 2, no. 3 (2021): 100372, https://doi.org/10.1016/j.xcrp.2021.100372.

14. S. Wagner, C. Weisenstein, A. D. Smith, M. Östling, S. Kataria, and M. C. Lemme, "Graphene Transfer Methods for the Fabrication of Membrane-Based NEMS Devices," *Microelectronic Engineering* 159 (2016): 108, https://doi.org/10.1016/j.mee.2016.02.065.

15. X. Langston and K. E. Whitener, "Graphene Transfer: A Physical Perspective," *Nanomaterials* 11, no. 11 (2021): 2837, https://doi.org/10.3390/nano11112837.

16. C. Mattevi, H. Kim, and M. Chhowalla, "A Review of Chemical Vapour Deposition of Graphene on Copper," *Journal of Materials Chemistry* 21, no. 10 (2011): 3324, https://doi.org/10.1039/C0JM02126A.

17. D. Jin, W. Liu, L. Jia, et al., "Thickness- and Wavelength-Dependent Nonlinear Optical Absorption in 2D Layered MXene Films," *Small Science* 4, no. 8 (2024): 2400179, https://doi.org/10.1002/smsc.202400179.

18. X. Xu, Z. Zhang, J. Dong, et al., "Ultrafast Epitaxial Growth of Metre-Sized Single-Crystal Graphene on Industrial Cu Foil," *Science Bulletin* 62, no. 15 (2017): 1074, https://doi.org/10.1016/j.scib.2017.07.005.

19. T. Cheng, Z. Liu, Z. Liu, and F. Ding, "The Mechanism of Graphene Vapor–Solid Growth on Insulating Substrates," *ACS Nano* 15, no. 4 (2021): 7399, https://doi.org/10.1021/acsnano.1c00776.

20. J. Chen, Y. Wen, Y. Guo, et al., "Oxygen-Aided Synthesis of Polycrystalline Graphene on Silicon Dioxide Substrates," *Journal of the American Chemical Society* 133, no. 44 (2011): 17548, https://doi.org/10.1021/ja2063633.

21. M. Son, H. Lim, M. Hong, and H. C. Choi, "Direct Growth of Graphene Pad on Exfoliated Hexagonal Boron Nitride Surface," *Nanoscale* 3, no. 8 (2011): 3089, https://doi.org/10.1039/C1NR10504C.

22. K. Saito and T. Ogino, "Direct Growth of Graphene Films on Sapphire, 0001 and $(11\bar{2}0)$ Surfaces by Self-Catalytic Chemical Vapor Deposition," *Journal of Physical Chemistry C* 118 (2014): 5523, https://doi.org/10.1021/jp408126e.

23. J. Sun, T. Gao, X. Song, et al., "Direct Growth of High-Quality Graphene on High-κ Dielectric $SrTiO_3$ Substrates," *Journal of the American Chemical Society* 136, no. 18 (2014): 6574, https://doi.org/10.1021/ja5022602.

24. Z. Chen, B. Guan, X.-d. Chen, et al., "Fast and Uniform Growth of Graphene Glass Using Confined-Flow Chemical Vapor Deposition and Its Unique Applications," *Nano Research* 9, no. 10 (2016): 3048, https://doi.org/10.1007/s12274-016-1187-6.

25. Q. Liu, Y. Gong, T. Wang, W.-L. Chan, and J. Wu, "Metal-Catalyst-Free and Controllable Growth of High-Quality Monolayer and AB-Stacked Bilayer Graphene on Silicon Dioxide," *Carbon* 96 (2016): 203, https://doi.org/10.1016/j.carbon.2015.09.075.

26. H. Ago, Y. Ito, N. Mizuta, et al., "Epitaxial Chemical Vapor Deposition Growth of Single-Layer Graphene over Cobalt Film Crystallized on Sapphire," *ACS Nano* 4, no. 12 (2010): 7407, https://doi.org/10.1021/nn102519b.

27. C.-J. Chang, P.-C. Tsai, W.-Y. Su, C.-Y. Huang, P.-T. Lee, and S.-Y. Lin, "Layered Graphene Growth Directly on Sapphire Substrates for Applications," *ACS Omega* 7, no. 15 (2022): 13128, https://doi.org/10.1021/acsomega.2c00554.

28. A. C. Ferrari and D. M. Basko, "Raman Spectroscopy as a Versatile Tool for Studying the Properties of Graphene," *Nature Nanotechnology* 8, no. 4 (2013): 235, https://doi.org/10.1038/nnano.2013.46.

29. S. Shrestha, C. S. Chang, S. Lee, et al., "Raman Spectroscopic Characterizations of Graphene on Oxide Substrates for Remote Epitaxy," *Journal of Applied Physics* 133, no. 10 (2023): 105301, https://doi.org/10.1063/5.0143083.

30. C. Neumann, S. Reichardt, P. Venezuela, et al., "Raman Spectroscopy as Probe of Nanometre-Scale Strain Variations in Graphene," *Nature Communications* 6, no. 1 (2015): 8429, https://doi.org/10.1038/ncomms9429.

31. Y. y Wang, Z. h Ni, T. Yu, et al., "Raman Studies of Monolayer Graphene: The Substrate Effect," *The Journal of Physical Chemistry C* 112, no. 29 (2008): 10637, https://doi.org/10.1021/jp8008404.

32. S. D. Costa, A. Righi, C. Fantini, et al., "Resonant Raman Spectroscopy of Graphene Grown on Copper Substrates," *Solid State Communications* 152, no. 15 (2012): 1317, https://doi.org/10.1016/j.ssc.2012.05.001.

33. B. J. Schultz, C. J. Patridge, V. Lee, et al., "Imaging Local Electronic Corrugations and Doped Regions in Graphene," *Nature Communications* 2, no. 1 (2011): 372, https://doi.org/10.1038/ncomms1376.

34. J. Stöhr, NEXAFS Spectroscopy, Springer Series in Surface Sciences (Springer, 2013), ISBN 3662028530.

35. L. L. Rusevich, M. Tyunina, E. A. Kotomin, N. Nepomniashchaia, and A. Dejneka, "The Electronic Properties of $SrTiO_3$-δ with Oxygen

Vacancies or Substitutions," *Scientific Reports* 11, no. 1 (2021): 23341, https://doi.org/10.1038/s41598-021-02751-9.

36. Z. Chen, C. Xie, W. Wang, et al., "Direct Growth of Wafer-Scale Highly Oriented Graphene on Sapphire," *Science Advances* 7, no. 47 (2021): eabk0115, https://doi.org/10.1126/sciadv.abk0115.

37. B. Vasić, A. Zurutuza, and R. Gajić, "Spatial Variation of Wear and Electrical Properties across Wrinkles in Chemical Vapour Deposition Graphene," *Carbon* 102 (2016): 304, https://doi.org/10.1016/j.carbon.2016.02.066.

38. K. S. Park, S. Kim, H. Kim, et al., "Wafer-Scale Single-Domain-Like Graphene by Defect-Selective Atomic Layer Deposition of Hexagonal ZnO," *Nanoscale* 7, no. 42 (2015): 17702, https://doi.org/10.1039/C5NR05392G.

39. B. Deng, Z. Pang, S. Chen, et al., "Wrinkle-Free Single-Crystal Graphene Wafer Grown on Strain-Engineered Substrates," *ACS Nano* 11, no. 12 (2017): 12337, https://doi.org/10.1021/acsnano.7b06196.

40. P. Pranav Pradeep, P. C. Shyni, V. Gopal, S. G. Bhat, and P. S. A. Kumar, "LSAT (001) Termination: An Investigation on the Influence of Annealing Parameters on Topography," *Physica B: Condensed Matter* 640 (2022): 414092, https://doi.org/10.1016/j.physb.2022.414092.

41. A. Dobrowolski, J. Jagiełło, K. Piętak-Jurczak, M. Wzorek, D. Czołak, and T. Ciuk, "Spectroscopic Properties of Close-to-Perfect-Monolayer Quasi-Free-Standing Epitaxial Graphene on 6HSiC(0001)," *Applied Surface Science* 642 (2024): 158617, https://doi.org/10.1016/j.apsusc.2023.158617.

42. Y. Fukaya, S. Entani, S. Sakai, et al., "Spacing between Graphene and Metal Substrates Studied with Total-Reflection High-Energy Positron Diffraction," *Carbon* 103 (2016): 1, https://doi.org/10.1016/j.carbon.2016.03.006.

43. Z. Ao, M. Jiang, Z. Wen, and S. Li, "Density Functional Theory Calculations on Graphene/α-$SiO_2$0001 Interface," *Nanoscale Research Letters* 7, no. 1 (2012): 158, https://doi.org/10.1186/1556-276X-7-158.

44. Q. Wang, S. Yan, B. Dong, et al., "Preparation of Environmentally Friendly High-Emissivity Ca^{2+}-Fe^{3+} Co-Doped $LaAlO_3$ Ceramic," *International Journal of Applied Ceramic Technology* 20, no. 3 (2023): 1785, https://doi.org/10.1111/ijac.14335.

45. Y. Lu, D. Jia, F. Gao, T. Hu, and Z. Chen, "First-Principle Calculations of the Thermal Properties of $SrTiO_3$ and $SrO(SrTiO_3)n$ (n=1,2)," *Solid State Communications* 201 (2015): 25, https://doi.org/10.1016/j.ssc.2014.09.011.

46. W. Bao, F. Miao, Z. Chen, et al., "Controlled Ripple Texturing of Suspended Graphene and Ultrathin Graphite Membranes," *Nature Nanotechnology* 4, no. 9 (2009): 562, https://doi.org/10.1038/nnano.2009.191.

47. X. Li, W. Cai, J. An, et al., "Large-Area Synthesis of High-Quality and Uniform Graphene Films on Copper Foils," *Science* 324, no. 5932 (2009): 1312, https://doi.org/10.1126/science.1171245.

48. H. Wang, X. Xue, Q. Jiang, et al., "Primary Nucleation-Dominated Chemical Vapor Deposition Growth for Uniform Graphene Monolayers on Dielectric Substrate," *Journal of the American Chemical Society* 141, no. 28 (2019): 11004, https://doi.org/10.1021/jacs.9b05705.

49. S. Bhaviripudi, X. Jia, M. S. Dresselhaus, and J. Kong, "Role of Kinetic Factors in Chemical Vapor Deposition Synthesis of Uniform Large Area Graphene Using Copper Catalyst," *Nano Letters* 10, no. 10 (2010): 4128, https://doi.org/10.1021/nl102355e.

50. I. R. Hamdani, A. Ahmad, H. M. Chulliyil, C. Srinivasakannan, A. A. Shoaibi, and M. M. Hossain, "Thermocatalytic Decomposition of Methane: A Review on Carbon-Based Catalysts," *ACS Omega* 8, no. 32 (2023): 28945, https://doi.org/10.1021/acsomega.3c01936.

51. H. F. Abbas and W. M. A. Wan Daud, "Hydrogen Production by Methane Decomposition: A Review," *International Journal of Hydrogen Energy* 35, no. 3 (2010): 1160, https://doi.org/10.1016/j.ijhydene.2009.11.036.

52. H. F. Abbas and W. M. A. W. Daud, "Hydrogen Production by Thermocatalytic Decomposition of Methane Using a Fixed Bed Activated Carbon in a Pilot Scale Unit: Apparent Kinetic, Deactivation and Diffusional Limitation Studies," *International Journal of Hydrogen Energy* 35, no. 22 (2010): 12268, https://doi.org/10.1016/j.ijhydene.2010.08.036.

53. G. Shirane and Y. Yamada, "Lattice-Dynamical Study of the 110°K Phase Transition in $SrTiO_3$," *Physical Review* 177, no. 2 (1969): 858, https://doi.org/10.1103/PhysRev.177.858.

54. F. W. Lytle, "X-Ray Diffractometry of Low-Temperature Phase Transformations in Strontium Titanate," *Journal of Applied Physics* 35, no. 7 (1964): 2212, https://doi.org/10.1063/1.1702820.

55. H. Unoki and T. Sakudo, "Electron Spin Resonance of Fe^{3+} in $SrTiO_3$ with Special Reference to the 110°K Phase Transition," *Journal of the Physical Society of Japan* 23, no. 3 (1967): 546, https://doi.org/10.1143/JPSJ.23.546.

56. H. W. Kim, W. Ko, J. Ku, et al., "Nanoscale Control of Phonon Excitations in Graphene," *Nature Communications* 6, no. 1 (2015): 7528, https://doi.org/10.1038/ncomms8528.

57. Y. Zhang, V. W. Brar, F. Wang, et al., "Giant Phonon-Induced Conductance in Scanning Tunnelling Spectroscopy of Gate-Tunable Graphene," *Nature Physics* 4, no. 8 (2008): 627, https://doi.org/10.1038/nphys1022.

58. T. O. Wehling, I. Grigorenko, A. I. Lichtenstein, and A. V. Balatsky, "Phonon-Mediated Tunneling into Graphene," *Physical Review Letters* 101, no. 21 (2008): 216803, https://doi.org/10.1103/PhysRevLett.101.216803.

59. S. Woo, H. Jeong, S. A. Lee, et al., "Surface Properties of Atomically Flat Poly-Crystalline $SrTiO_3$," *Scientific Reports* 5, no. 1 (2015): 8822, https://doi.org/10.1038/srep08822.

Supporting Information

Additional supporting information can be found online in the Supporting Information Section. **Supporting Fig. S1**: Subtraction of substrate Raman spectra from raw Raman spectra to isolate graphene features. Substrate spectra were collected at same locations as the raw spectra. (a) Gr/STO, (b) Gr/LAO, (c) Gr/LSAT HHs. **Supporting Fig. S2**: Large-area optical microscopy images of (a) Gr/STO and (b) Gr/LAO HHs. The images demonstrate the high uniformity and absence of large-scale defects, particulates, or delaminated regions across the 5×5 mm^2 sample surfaces. **Supporting Fig. S3**: Statistical analyses of Raman spectra for (a) Gr/STO and (b) Gr/LAO HHs. The solid lines and the corresponding color-shaded regions represent the average and standard deviation of the Raman spectra on different positions of the HH. **Supporting Fig. S4**: Raman spectra, TEM, and STEM characterization of Gr/LSAT HH. (a) Raman spectra from 16 evenly spaced points on the Gr/LSAT HH. (b) TEM and (c) STEM images of Gr/LSAT. Dark lines in both images (highlighted by horizontal yellow lines) indicate monolayer graphene. **Supporting Fig. S5**: G and D peak intensity maps from Raman spectroscopy. (a,b) Gr/STO, (c,d) Gr/LAO. Uniform G peak intensity maps (a,c) confirm consistent graphene coverage. **Supporting Fig. S6**: C *K*-edge NEXAFS spectra of the HHs. All samples exhibit σ* C=C bonding at 292 eV and π* C-C bonding at 286 eV of graphene. Broadening between these bands indicates potential interlayer or adsorbate-induced features. **Supporting Fig. S7**: SEM images of growth in improper APCVD conditions. (a,b) Growth at high temperature and high precursor flow rate, showing defects as bright spots. (c) Overgrown graphene image when the substrate's growth position is near the outlet side of the APCVD chamber. **Supporting Fig. S8**: AFM analysis of graphene wrinkles and substrate steps. (a–d) Topography of Gr/STO, Gr/LAO, and Gr/LSAT HHs. (e–j) Line profiles along the arrows show comparable wrinkle (blue lines) (e–g) and step heights (navy lines) (h–j) for the HHs. **Supporting Fig. S9**: AFM topography images of pristine substrate: (a) STO and (b) LAO show flat step-terrace structures; (c) LSAT shows pits and mounds from surface SrO segregation.

Supporting Fig. S10: LFM images of HHs of Gr/STO (a) and Gr/ LAO (b). Increased friction observed at graphene wrinkles and substrate step edges. **Supporting Fig. S11**: C-AFM images of Gr/STO. (a,b) AFM topography and (c,d) current maps with line profile from identical regions, revealing local conductivity variations. **Supporting Fig. S12**: Cross-sectional STEM of multilayer (defective) regions. (a) Gr/STO, (b) Gr/LAO showing bilayer graphene (yellow lines). (c) SEM and (d) STEM near defects (yellow circle) showing trilayer graphene. **Supporting Fig. S13**: TEM (a) and STEM (b) images of a graphene wrinkle on Gr/STO. Wrinkle height is 1.4 nm, consistent with AFM profiles. **Supporting Fig. S14**: Raman spectra of HHs grown at different temperatures. (a) Gr/STO and (b) Gr/LAO with temperature labels. **Supporting Fig. S15**: AFM of HHs grown at 1100 °C. Left column (a,c,e): 1 h growth; right column (b,d,f): 4 h growth for Gr/STO, Gr/LAO, and Gr/LSAT, respectively. **Supporting Fig. S16**: AFM of HHs grown at optimal 1070 °C. (a,c): 1h; (b,d): 3h. (a,b) Gr/STO; (c,d) Gr/LAO. **Supporting Fig. S17**: Effect of H2 flow rate on Gr/STO. (a – d) AFM images at 100, 40, 10, 5, and 0 sccm. (e) Optical images showing full carbon foil coverage at 0 sccm. (f) Corresponding Raman spectra. **Supporting Fig. S18**: Gr/STO grown at 16 sccm CH4. (a) AFM and (b) SEM images showing adlayers (white and dark spots). **Supporting Fig. S19**: Low temperature Raman spectra of Gr/LAO HH. (a,b) G and 2D peak contour plots. (c,d) Peak positions. **Supporting Fig. S20**: NEXAFS spectra of the Ti L-edge and O K-edge for various samples. (a) Ti L-edge spectra comparing the as-grown Gr/STO sample (red) with a control Gr/STO sample annealed in oxygen to restore stoichiometry (black). (b) O K-edge spectra for Gr/LSAT (green), Gr/LAO (blue). The Ti L-edge spectra for both as-grown and annealed Gr/STO samples are virtually identical and lack any distinct features corresponding to Ti^{3+}species. The O K-edge spectra also show highly similar features between STO and STO OV sample.